JOURNAL OF MATERIALS SCIENCE 20 (1985) 1033–1048

Shock compaction of silicon carbide powder

KEN-ICHI KONDO, SINJI SOGA, AKIRA SAWAOKA
Research Laboratory of Engineering Materials, Tokyo Institute of Technology, 4259 Nagatsuta, Midori, Yokohama 227, Japan

MASATADA ARAKI
Nippon Oil and Fats Co, Ltd, Taketoyo Factory, 82 Aza-Nishimon, Taketoyo, Chita, Aichi 470-23, Japan

A series of shock compaction experiments on SiC powder were carried out over a wide range of shock pressures and shock temperatures up to 30 GPa and 3400 K. Large changes in some physical properties and a variety of unique microstructures were observed in the shock-treated samples with changes in impact conditions. For an iron plate impactor, the optimum impact condition, which depends on the initial density, is 2.5 km sec^{-1} for 70% initial density and 2.0 km sec^{-1} for 50%. The best-sintered compact of SiC with 97% density and micro-Vicker's hardness of 2700 kg mm^{-2} was obtained under optimum conditions. Good compacts with high relative density and high strength exhibit the disruptive effects of the shock wave, which are indicated by microstrain increase and crystallite size reduction. The skin model is presented here in order to estimate the heterogeneous shock state which is realized under and after shock loading of the initial powder aggregates.

1. Introduction

Shock waves in condensed matter have two effects on material; one is the production of disruptive forces within the shock front and the other the production of bonding forces due to high stresses and high temperatures. Both of these are, of course, strongly related to the chemical effects of the passage of a shock wave. Recently, a shock compaction technique making the best use of these effects is expected to be established in the field of powder consolidation or fabrication because of its unique potentials and advantages, for example, possible application to difficult-to-compact metals and ceramics, unstable materials, unique microstructure materials, and so on [1–4].

For normal and rapidly solidified metallic powders, some successful results on shock compaction have already been reported [5–7]. On the other hand, shock compaction experiments for ceramic powders have given rise to prominent undesirable effects, such as macroscopic and microscopic cracking and remaining pores [8–12]. The cracking phenomena are dependent on the nature of the material, the state of the powders prior to compaction, shock-wave geometries, etc., and are not well understood. The difficulties in shock compaction of ceramic powders are primarily caused by the brittle nature of ceramic powders. Difficulties in controlling precisely the shock states of initially porous materials and aggregates of powders also result in the above difficulties because of lack of understanding of the constitutive relations for such materials with these initial states [13–20].

We have reported on the disruptive forces of shock waves remaining in recovered materials such as MgO, Al_2O_3, BN, Si_3N_4, and TiN after shock treatment [21–23]. The macroscopic particle size reduction was determined by electron microscopy. The reduction of crystallite size and the increase of microstrain caused by shock compression were evaluated from X-ray line-broadening analysis

0022–2461/85 $03.00 + .12

based on the Hall's equation [22, 23]. The bonding effects of the shock wave intended for shock compaction and influences due both to the nature of chemical bonding and the physical properties of material have been examined for TiN–TiC solid solution system by the authors [24]. However, influences of changes in shock pressure and shock temperature were obscure in these experiments. In order to overcome serious deficiencies of basic understanding of the shock compaction phenomena, a systematic study is required.

In the present paper, one of the series of shock recovery experiments of SiC powder is described, aiming at the determination of the influences due to both changes in shock pressure and shock temperature and their distributions in the sample. The distributions realize the heterogeneous state under and after shock loading. The present authors have proposed a model for such a heterogeneous shock state.

2. Experimental details

Silicon carbide (SiC) powder used as a starting material is of stock commercial grade, Betarundum (Ultrafine grade), which was supplied by Ibiden Co, Ltd. The powder is of cubic structure, β-SiC but includes a small amount of α-phase, approximately 2 to 4%. Characteristics of the powder are shown in Table I. Particle shape of the powder is uniform and spherical, as shown in Fig. 1. The powders were pressed into a stainless steel capsule, as shown in Fig. 2. The capsule is in the shape of a column 30 mm in length and 24 mm in diameter with a small hole allowing the evacuation of air from the inside of the capsule before tightening the plug. The amount of powder charged and packing pressure were changed so as to obtain three relative densities, approximately 30, 50 and 70%. When evacuated, the capsule was heated at approximately 200° C for 30 min using a hot plate, sealed with silicone rubber applied to the screw of

TABLE I Characteristics of SiC starting powder

Average particle size	0.28 μm
Maximum particle size	1.7 μm
Particles under 1 μm	95.8%
Specific surface area	18.7 $m^2 g^{-1}$
Impurities	
free SiO_2	0.34 wt%
free C	0.51 wt%
total Al	0.02 wt%
total Fe	0.07 wt%
H_2O	0.209 wt%

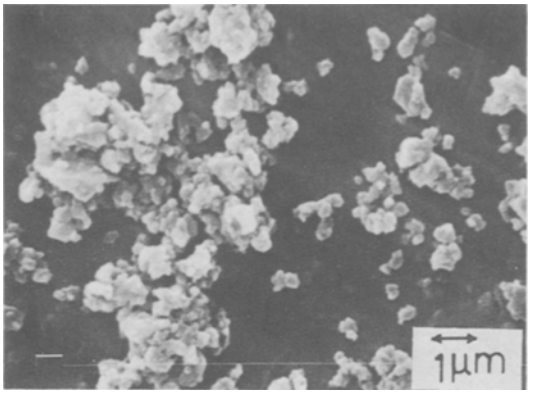

Figure 1 SEM Photograph of SiC starting powder used.

the plug, and then the plug was tightened. The sample space in the capsule was 12 mm in diameter and 5 mm in height. Three capsules with different densities of sample were set in a momentum-trap assembly and simultaneously impacted by an explosively driven flyer plate of iron 3.2 mm in thickness, where a mouse-trap type plane-wave generator was used [22]. The momentum-trap assembly, consisting of three pieces of iron ring and plates, was 120 mm in diameter and 60 mm in height. Impact velocities of the flyer were 1.5, 2, 2.5 and 3 1km sec^{-1}, to which the generated shock pressures of 32, 45, 60 and 77 GPa for the capsule material of SUS 304 stainless steel corresponded, respectively. Pressures in the samples were

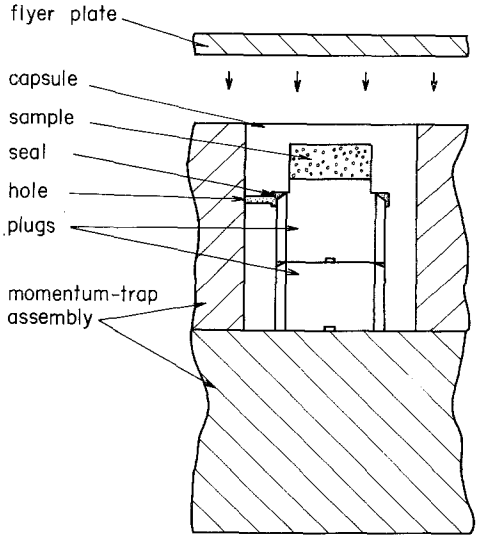

Figure 2 Cross-section of a stainless steel capsule and a momentum-trap assembly for shock compaction experiments using an explosively driven flat-flyer plate technique.

TABLE II Summary of experimental conditions and results

Sample number	Flyer velocity (km sec^{-1})	Initial density (%)	Shock pressure (GPa)	Shock temperature (K)	Relative density (%)	Vicker's hardness (kg mm^{-2})	Core temperature (K)
4.1	1.5	70	9.4	970	94.9	1570	315
4.2	1.5	50	5.1	1100	92.6	2410	307
4.3	1.5	30	2.4	1200	94.9	1280	–
5.1	2.0	70	15.3	1350	96.2	2320	331
5.2	2.0	50	8.7	1600	95.8	2640	314
5.3	2.0	30	4.0	1760	–	–	–
6.1	2.5	70	22.2	1780	96.8	2730	355
6.2	2.5	50	13.2	2200	93.9	2360	325
6.3	2.5	30	6.3	2500	–	–	–
7.1	3.0	70	29.9	2280	89.4	2180	392
7.2	3.0	50	18.4	2910	88.8	2530	341
7.3	3.0	30	9.2	3400	–	–	–

different from these capsule pressures, as described later. After impact, everything was driven into a water basin and then recovered from the water. The experimental conditions are summarized in Table II.

After the shock treatment, samples were recovered by carefully shaving off the capsule material with a lathe. Most of the samples were consolidated and it was possible to handle them, but some were not. Apparent density of the shock-compacted samples was measured by an Archimedean technique using water and paraffin to coat the sample. Surfaces of the shock-compacted samples were polished with diamond powder and mirror-like shining surfaces were obtained. The micro-Vicker's hardness was measured at a 200 g load for 10 sec. Fracture surfaces of all the samples were observed by a scanning electron microscope. X-ray diffraction experiments on the samples crushed by an agate mortar were carried out. A lattice parameter of the shock-treated samples was obtained by a least-squares fit to all the peaks of the diffraction patterns up to 80° in 2θ. The half-maximum widths of the diffraction profiles were determined to obtain the values of microstrain and a crystallite size of the shock-treated samples, by using the Rachinger's correction method [25] and the Hall equation [22, 23, 26].

3. Shock state

With the assumption that a shock wave profile is steady in time, the well-known Rankine–Hugoniot equations have been developed, and they have usually been employed to determine the shock state. These equations relate such parameters as pressure (P), internal energy (E), and specific volume (V) or density (ρ) behind the shock wave to these same quantities in front of the shock wave in terms of the shock velocity (u_s) and the particle velocity (u_p) due to the shock wave [27]. These equations are derived from the conservation relationships of mass, momentum, and energy. For a coordinate system in which the material in front of the shock wave is at rest, they are

$$P = \rho_0 u_s u_p, \tag{1}$$

$$1 - V/V_0 = u_p/u_s, \tag{2}$$

$$E - E_0 = P(V_0 - V)/2 \tag{3}$$

where the subscript zero represents values under ambient conditions.

Hugoniot compression data of fully sintered (initial density of 3.1 Mg m^{-3}) and porous (initial density of 2.3 Mg m^{-3}) SiC were obtained by McQueen *et al.* [27]. The former is almost the crystal density of SiC. In order to determine the actual shock pressure and temperature in the samples, it is necessary to calculate Hugoniot compression curves of the porous samples with a corresponding porosity. It is usually assumed that the thermodynamic equilibrium state is achieved in the shock-compressed matter behind the shock wave front. The following equation, based on the Mie–Grüneisen equation of state, relates the pressure and energy at any particular volume to these quantities on the Hugoniot through some average value of the Grüneisen parameter (γ),

$$E = E_H + (P - P_H)/\rho\gamma, \tag{4}$$

where

$$\rho\gamma = (\partial P/\partial E)_V. \tag{5}$$

Using Equations 4 and 5 and assuming the thermodynamic equilibrium state, it is possible to compute the Hugoniot of the porous material from the crystal density or actual Hugoniot data as follows:

$$P^* = P[1-\rho\gamma(V_0-V)/2]/[1-\rho\gamma(V_0^*-V)/2], \quad (6)$$

where the asterisk denotes the porous material. The equation gives the pressure as a function of volume for a porous material centred at a volume V_0^* in terms of its reference Hugoniot. The shock velocity u_s^* and the particle velocity u_p^* for the porous material can be expressed as follows:

$$u_s^* = V_0^* \sqrt{P^*/(V_0^*-V)}, \quad (7)$$

$$u_p^* = \sqrt{(P^*(V_0^*-V)}. \quad (8)$$

These equations are applicable where the rigidity of the material and compression path, which are important in a relatively low pressure region, can both be ignored, and also where the volume of porous material under compression is smaller than the crystal density. The shock state experimentally achieved here was estimated by the impedance match solution using the published Hugoniot data [27] of steel, stainless steel (SUS 304), and the calculated porous Hugoniot of SiC.

According to a distance–time analysis for one-dimensional shock-wave propagation in the direction perpendicular to the flyer plate, shock reverberations might not occur between the sample and the capsule. However, the reflected shock wave from the inside wall of the capsule parallel to the direction of the shock-wave propagation must penetrate into the sample. Since this effect is too complicated to analyse, it is ignored here.

Under the thermodynamic equilibrium assumption, calculations of shock temperature are also possible on the basis of the Mie–Grüneisen equation of state. The shock temperature was actually estimated by the following equations which referred to the isentrope,

$$E^* = -\int_{V_0}^{V} P_s \mathrm{d}V + \int_{P_s}^{P^*} (\rho\gamma)^{-1}\mathrm{d}P, \quad (9)$$

$$\int_{T_s}^{T^*} C_V \mathrm{d}T = \int_{P_s}^{P^*} (\rho\gamma)^{-1}\mathrm{d}P, \quad (10)$$

and

$$T_s = T_0 \exp\left(-\int_{V_0}^{V} \rho\gamma \mathrm{d}V\right), \quad (11)$$

where subscript s represents the isentropic compression state at volume V, and C_V is the specific heat capacity [28]. Formulae of the Birch–Murnaghan second-order equation of state were used to represent the isentropic compression as follows:

$$P = \frac{3}{2}K_0\left[\left(\frac{V_0}{V}\right)^{\frac{7}{3}} - \left(\frac{V_0}{V}\right)^{\frac{5}{3}}\right]\left\{1+\frac{3}{4}(K_0'-4)\left[\left(\frac{V_0}{V}\right)^{\frac{2}{3}}-1\right]\right\} \quad (12)$$

where K_0 and K_0' are the bulk modulus and its pressure derivatives, respectively. The values for the both are related to the bulk sound velocity (C_0) and Grüneisen parameter (γ_0) determined by the shock experiments as follows:

$$K_0 = \rho_0 C_0^2. \quad (13)$$

and

$$K_0' = 2\gamma_0 + 1 \quad (14)$$

where the latter is based on the Dugdale–MacDonald assumption [29]. For the specific heat and the thermal energy, the Debye model was employed, where Debye temperature θ_D is 1140 K and dependent on volume as follows:

$$\gamma = -\left(\frac{\ln \theta_D}{\ln V}\right)_T. \quad (15)$$

The value of $\rho\gamma$ was assumed to be constant, 3.90×10^3 kg m^{-3}, which was determined experimentally [27]. This approximation is often employed in shock data analyses and is usually reasonable.

The estimated shock pressures and shock temperatures in SiC samples are also summarized in Table II. It is seen from Table II that the present experimental conditions are extended in the considerably wide pressure and temperature regions which are difficult to obtain by static methods.

Although it is difficult to determine the release adiabatic from the shock state to atmospheric pressure, the release path is probably close to the shock Hugoniot of crystal density SiC. Therefore, since volume expansion and energy for the expansion in the release process is relatively small, the post-shock temperature is close to the shock temperature. The post-shock temperature of the sample decreases through heat conduction in the

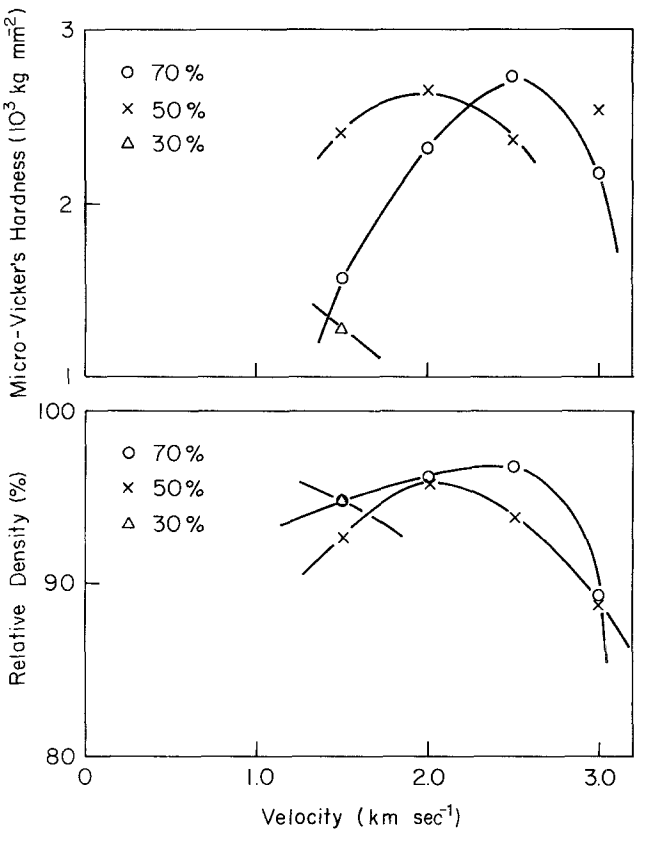

Figure 3 Relative density and micro-Vicker's hardness of shock-compacted bodies as a function of impactor velocity. The percentage in the figure denotes the initial density.

capsule wall made of stainless steel. It is estimated that it took approximately 4 sec to reach one third of the post-shock temperature in the experiments.

4. Results and discussion

Fig. 3 shows the relative density and micro-Vicker's hardness as a function of impact velocity with a parameter of the initial density. The sample with the initial density of 70% at an impact velocity of 2.5 km sec^{-1} is changed to the best compact with apparent density of 96.8% and micro-Vicker's hardness of 2730 kg mm^{-2}. The second best is obtained for the sample with initial density of 50% at an impact velocity of 2 km sec^{-1}, which shows an apparent density of 95.8% and micro-Vicker's hardness of 2640 kg mm^{-2}. The samples with 30% initial density are not compacted except that impacted at a velocity of 1.5 km sec^{-1}. Fig. 3 suggests as a general tendency that an appropriate impact velocity exists for a particular initial density. It is likely that the high value of micro-Vicker's hardness for the sample with initial density of 50% at an impact velocity of 3 km sec^{-1} is accidental, as compared to the low value of density.

Figs. 4 and 5 also show the relative density and micro-Vicker's hardness as a function of shock pressure and shock temperature in the sample, respectively. It is evident from Fig. 4 that the shock pressure for the maximum values of density and hardness is dependent on the initial density, but the shock temperature for those maxima is approximately constant at 1800 K, as shown in Fig. 5. Therefore, the shock temperature, rather than the shock pressure, seems to be the dominant factor for shock compaction. This is because the shock pressure is high enough to exceed both the yield strengths of the SiC powder particles and the bridge structures formed in the powder compact, and also because the shock state is in the third-stage region [2, 3], where the first, the second, and the third stages are classified as transitional re-stacking, plastic deformation, and cold working and/or particle fracture, respectively.

Typical scanning electron micrographs (SEM) are shown in Figs. 6 to 9, which correspond to samples of different densities impacted at 1.5, 2, 2.5, and 3 km sec^{-1}, respectively. A variety of microstructures can be seen as a response to the wide range of shock pressures and shock temperatures.

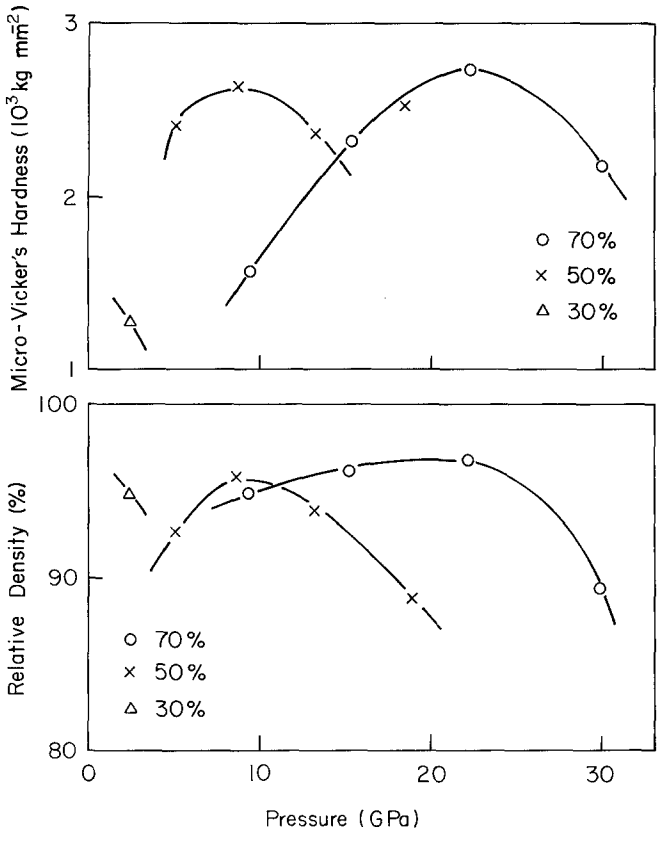

Figure 4 Relative density and micro-Vicker's hardness of shock-compacted bodies as a function of shock pressure. The percentage in the figure denotes the initial density. The maximum point depends on the initial density.

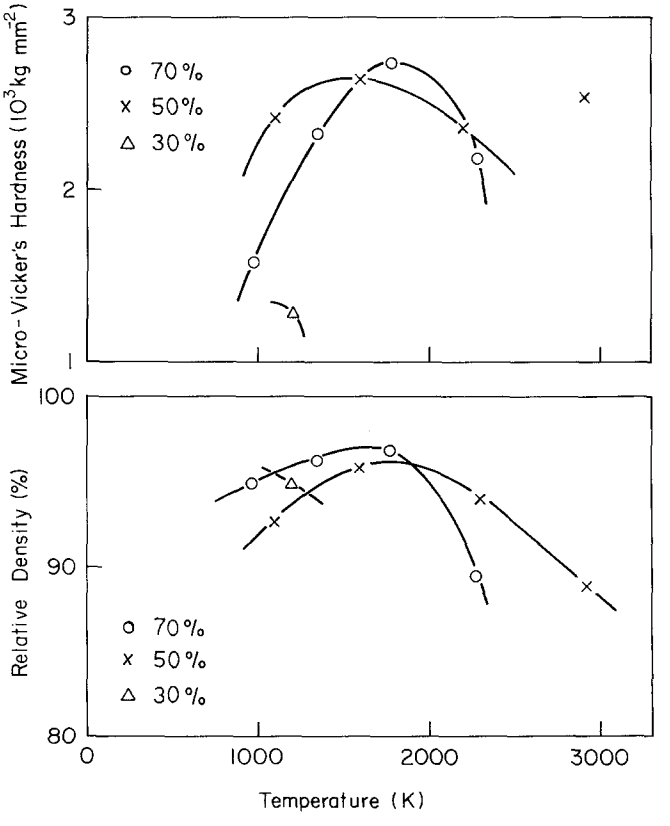

Figure 5 Relative density and micro-Vicker's hardness of shock-compacted bodies as a function of shock temperature. The percentage in the figure denotes the initial density. The maximum point is located at approximately 1800 K.

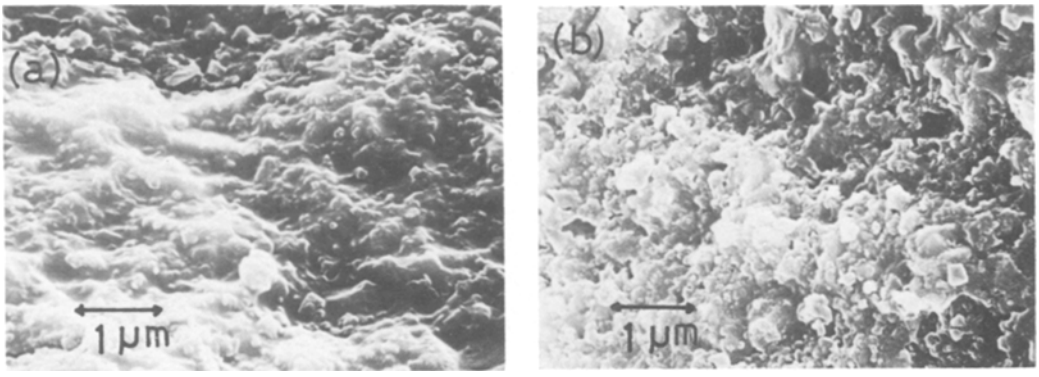

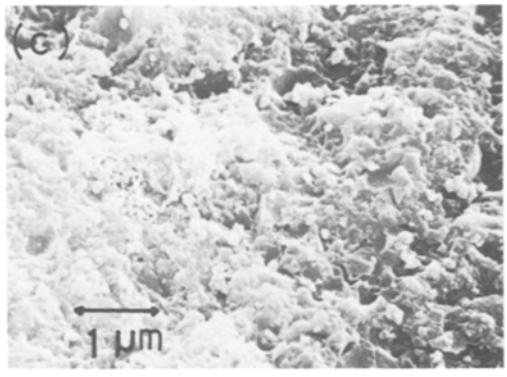

Figure 6 SEM photographs of the fractured surface of shock-compacted bodies which are impacted at a velocity of 1.5 km sec^{-1}. (a), (b), and (c) are for initial densities of 30, 50, and 70%, respectively.

The photograph for the sample with initial density of 30% in Fig. 6a shows that the original sub-micrometre particles are joined to each other by melted materials but the others with the initial density of 30% (Figs. 7a, 8a and 9a) clearly show recrystallization by which the particle size becomes 1 to 3 μm and relatively uniform. At the highest velocity impact, the recrystallized particles merely contact with others and indicate a twinned crystal shape like a macle of natural diamond crystal which is well developed in the (1 1 1) crystallographic plane. Those three seem to be recrystallized without high stresses.

On the other hand, the original particles can be seen in Fig. 6b, and seem to be partially melted. The original particles are joined well with each other, as shown in Fig. 7b, which corresponds to the second best compact. The microstructure is

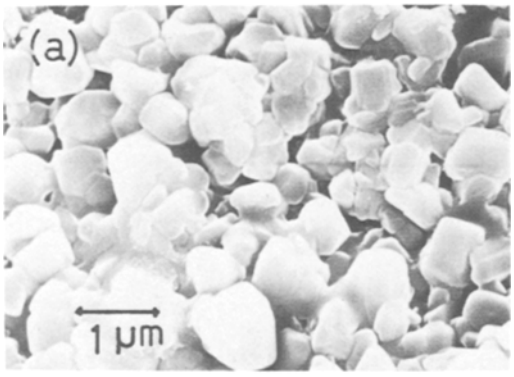

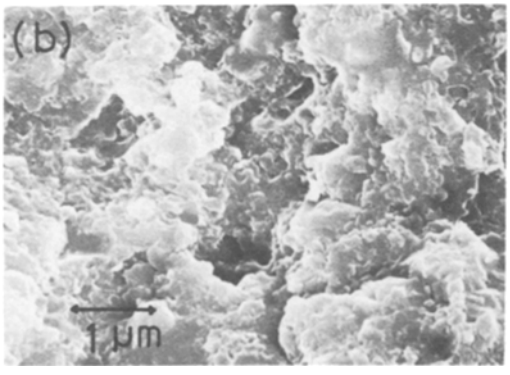

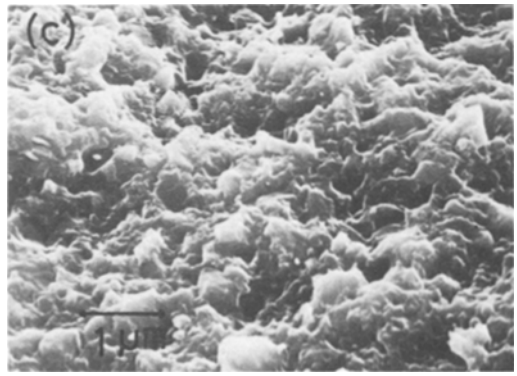

Figure 7 SEM photographs of the fractured surface of shock-compacted bodies which are impacted at a velocity of 2.0 km sec^{-1}. (a), (b), and (c) are for initial densities of 30, 50, and 70%, respectively.

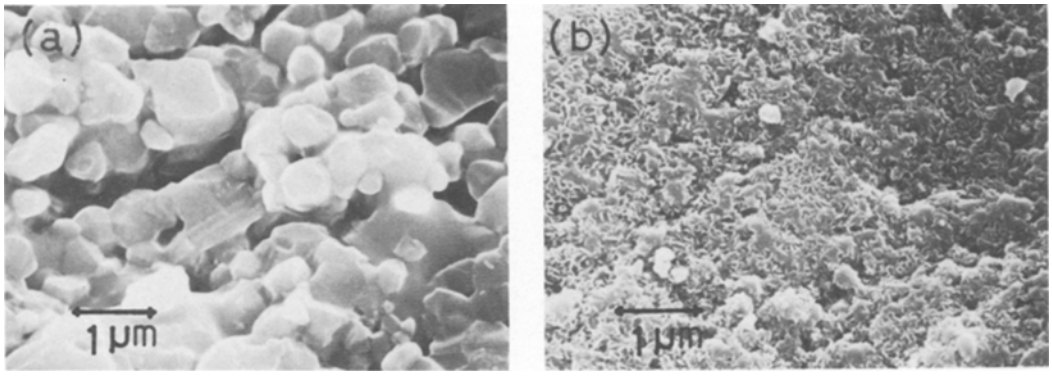

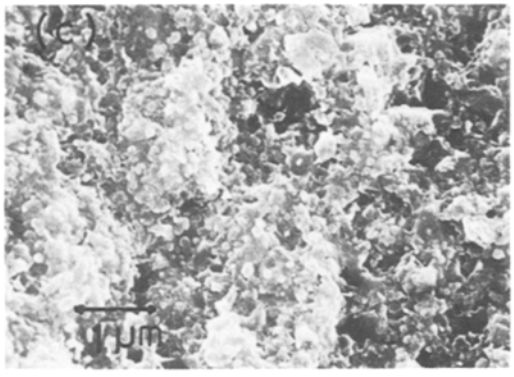

Figure 8 SEM photographs of the fractured surface of shock-compacted bodies which are impacted at a velocity of 2.5 km sec^{-1}. (a), (b), and (c) are for initial densities of 30, 50, and 70%, respectively.

relatively homogeneous, and it is difficult to distinguish grain boundaries. For samples with 70% initial density, very fine fragments, which are smaller than the original particles, can be seen in Fig. 6c, but at an impact velocity of 2 km sec^{-1} are melted to join the particles, as shown in Fig. 7c. The secondary particles with 1 μm size and a similar size of voids, which are made by removing the above particles at fracturing, can be seen in Fig. 7c.

A unique microstructure appears in the sample with initial density of 50% at an impact velocity of 2.5 km sec^{-1}, as shown in Fig. 8b. Sub-micrometre grains are joined with partially melted materials, and then form a rugged particle like an amoeba. A great number of small whisker-like crystals are produced on the surface of the secondary particles.

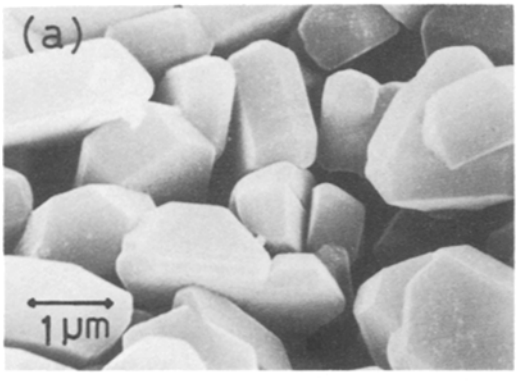

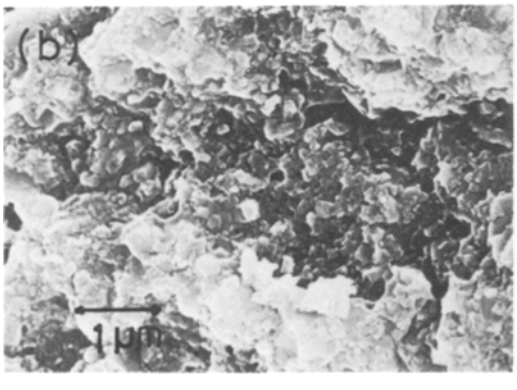

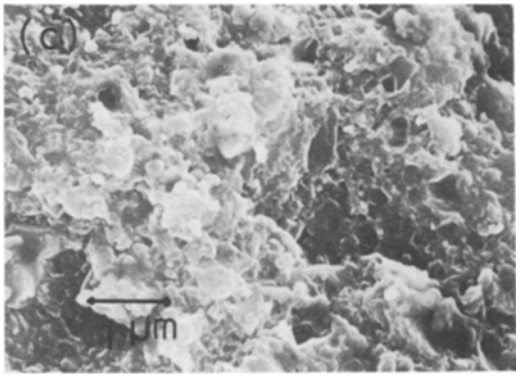

Figure 9 SEM photographs of the fractured surface of shock-compacted bodies which are impacted at a velocity of 3.0 km sec^{-1}. (a), (b), and (c) are for initial densities of 30, 50, and 70%, respectively.

TABLE III Crystallite size (L) and microstrain (ϵ) of shock-treated SiC determined by X-ray line-broadening analysis for different impact velocities

Porosity		1.5 km sec^{-1}		2.0 km sec^{-1}		2.5 km sec^{-1}		3.0 km sec^{-1}	
		L (nm)	ϵ (10^{-3})	L (nm)	ϵ (10^{-3})	L (nm)	ϵ (10^{-3})	L (nm)	ϵ (10^{-3})
70%	(a)	29.5	5.05	–	3.01	101	8.18	–	–
	(b)	31.5	7.09	–	7.84	60.0	9.09	–	3.55
50%	(a)	136	7.38	86.7	7.86	–	–	–	–
	(b)	83.0	8.85	66.0	9.24	–	2.74	–	–
30%	(a)	51.0	6.90	–	–	–	–	–	–
	(b)	42.7	8.75	–	1.36	–	–	–	–

(a) Compared with SiC starting powder.
(b) Compared with Al_2O_3 annealed powder.

They are approximately 5 nm in diameter and 50 nm in length. These are produced in the post-shock condition by rapid quenching of the liquid phase at the grain surfaces or by vapour deposition. This picture is evidence that a heterogeneous temperature distribution exists on the shock state. A photograph at a lower magnification showed periodic cracks every 50 μm. For the sample with initial density of 70% at an impact velocity of 2.5 km sec^{-1}, which corresponds to the compact with the best properties, 2 to 3 μm size clusters and small fragments can be seen in Fig. 8c. The size of cluster in Fig. 8c is almost same as that in Fig. 7b, and agrees with the recrystallized twin crystal shown in Fig. 9a. This is probably related to the initial size of the particle aggregates shown in Fig. 1. The microstructure shown in Fig. 8c seems to be considerably different from that in Fig. 7b, which corresponds to the second best compact. As shown in Fig. 4, this difference is caused by the large difference of shock pressure, 13.5 GPa, because the shock temperatures are almost same, as shown in Fig. 5. Samples with initial densities of 50 and 70% at an impact velocity of 3 km sec^{-1}, as shown in Figs. 9b and c, both exhibit large cracks by which the relative densities and micro-Vicker's hardness are decreased. As shown in Fig. 5, the decreases in these properties are due to the high shock temperature rather than the shock pressure because the pressure for Fig. 9b is lower than that for Fig. 8c, which corresponds to the best compact.

The crystal structure of the shock-compacted sample is determined by a powder X-ray diffraction technique and is not changed from β-SiC. The lattice parameters of the starting powder and all the shock-treated ones are 0.4369 + 0.0002 and 0.4374 + 0.0004 nm, respectively. The lattice parameter is increased a little by the shock treatment by which lattice distortions and/or lattice defects are produced, but is not essentially different from the starting powder. However, the line-broadening of the diffraction profiles is remarkable due to the shock treatment. Table III shows the crystallite size and the lattice distortion determined by using the Hall equation as referred to the starting SiC powder and well-annealed α-Al_2O_3 powder [22, 23]. Qualitatively, there is a clear correlation between annealing effects and impact velocities. Fig. 10 shows the experimental shock conditions in a pressure–temperature plane. The solid line indicates the boundary between the regions of annealing effects and disruptive effects. The lattice distortions and the crystallite size reductions remain in the samples recovered from the lower region, while the samples from the upper region are annealed to reduce lattice distortions and to increase the crystallite size as compared to those in the starting powder. The three samples for each initial density just above the line are more annealed than the starting powder, but still indicate microstrain as compared to the profiles from the well-annealed alumina. The broken line indicates the liquidus–solidus phase boundary which was empirically estimated by Van Vechten [30]. Since it is clear from Fig. 10 that the six samples with increasing microstrain were located in the solid phase region, the melting curve is consistent with the present data. It is, however, not clear whether the other samples are thermally annealed in the shock state or the post-shock state because it is difficult to confirm the sign of the pressure dependence of melting temperature from the data obtained here. As shown in Figs. 7a and 8a, the microstructures of the samples with 30% initial density at impact velocities of 2.0 and

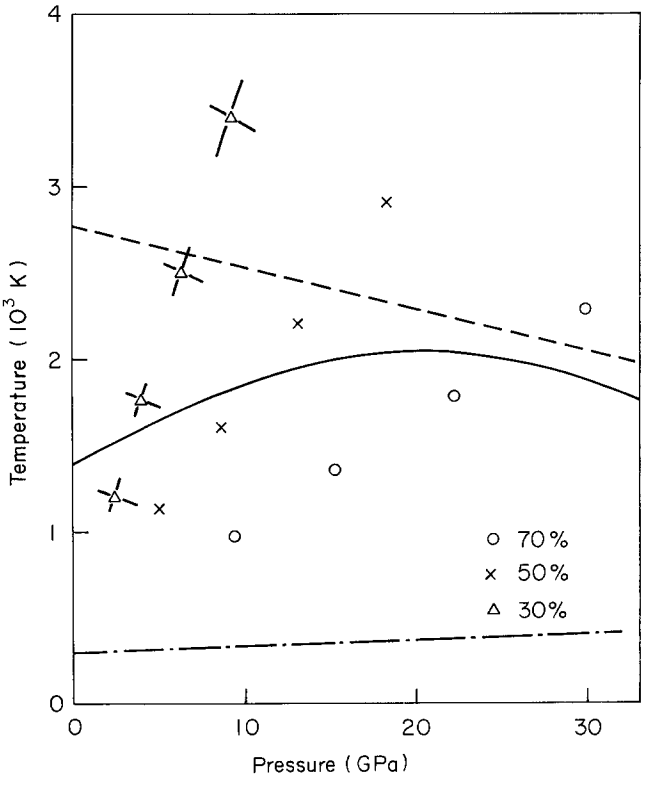

Figure 10 Experimental conditions shown in the pressure–temperature plane. The percentage in the figure denotes the initial density. The increase in pressure and temperature at a particular initial density corresponds to the increase in impactor velocity. The dashed line indicates the fusion curve of SiC estimated empirically by Van Vechten [30]. The solid line indicates the boundary between the regions of annealing effects (lower) and disruptive effects (upper). The dot-dashed line indicates the core temperature of the skin model as a function of shock pressure.

2.5 km sec^{-1} are not so different that both the samples might be melted. If so, the shock- and the post-shock-temperatures for the samples with initial density of 30% might be underestimated, and there remains a possibility of positive pressure dependence of melting temperature. In any case, α-phase (hexagonal) SiC is usually known as a high temperature phase just below the melting temperature. Since all the recovered materials are β-phase (cubic), the phase diagram of SiC in these regions would be actually more complicated than that suggested by Van Vechten [30].

According to the established Hugoniot of SiC obtained by McQueen *et al.* [27], the shock velocity decreases with increasing particle velocity up to 1.5 km sec^{-1} and increases linearly with increasing particle velocity over 1.5 km sec^{-1}. The interpolation to zero particle velocity along the linear relationship between shock velocity and particle velocity mentioned above corresponds to the bulk sound velocity in SiC crystal and suggests no phase change even at shock pressures over 50 GPa. The negative slope on the u_s–u_p plane suggests that the rigidity of SiC still remains at such high pressure or that softening of bulk elasticity occurs with increasing pressure. In order to determine which is correct or to determine the possibility of phase change, it is necessary to observe the shock-wave profile. For example, an in-material gauge like the one in the fused quartz and sintered AlN experiments is available [31, 32], where a ramp precursor-wave exists in front of the final shock wave. Therefore, the linear relationship between shock velocity and particle velocity is assumed in this paper, so that the estimated shock temperature contains some ambiguity.

It is clear from the SEM photographs that all samples except for those with initial density of 30% are partially melted rather than fully melted. In particular, it is clearly seen that the sample shown in Fig. 8b is partially melted on the particle surfaces and that nucleation just occurring on the melted surfaces is quenched. Therefore, we should consider that the shock temperatures must be different at the particle surface and the inside of particles. There is much evidence for such a heterogeneous temperature distribution induced by shock compression.

It has long been known that when a shock wave passes through a junction interface of two different metals, an anomalously large shock-induced electromotive force is produced [33]. This phenomenon is, however, mainly caused by local high temperatures at the junction with a porous

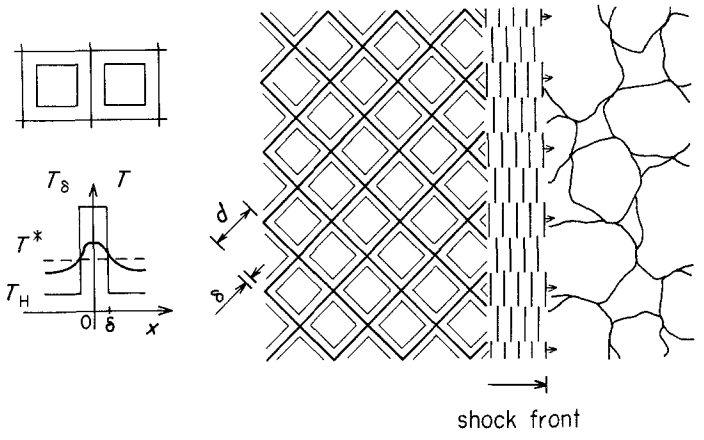

Figure 11 Schematic illustration for the skin model. The initial powder aggregates are transformed to the closely-packed cubes with a relatively thin skin through a shock front. Crystals of the core inside of the skin are isentropically-compressed or shock-compressed as the full density material, and the skin includes all the ambigious effects due to both the initial porous state and the complicated shock process. The mechanical equilibrium is achieved after passage of the shock front but a square temperature distribution at the skin remains. d and δ are dimension of the cube and thickness of the skin, respectively. T_δ, T_H, and T^* are the skin temperature, the core temperature, and the equilibrium temperature shown in Fig. 10, respectively.

layer [34, 35]. Since the porous layer at the junction is more compressible than the other, the increase of internal energy becomes much larger than that of the metals at the same pressure produced by the passage of a shock wave. The local high temperature and the subsequent thermal relaxation are explained well by a simple model, where the spatial and time behaviour of an initial "square" temperature distribution is governed by the one-dimensional thermal diffusion equation [36]. The problem of local heating in a heterogeneous system such as the junction of two metals is also very important, and exists in powder compacts in which there are many pores and loose contacts.

A similar problem occurs even in an initially homogeneous material. Recently, experimental evidence of heterogeneous temperature distribution has been presented by Kondo and Ahrens [37] via shock-induced thermal radiation measurements. The resultant colour temperatures are very high with a small value of emissivity, which is caused by a structure of the hot spot and/or shear band in the material due to heterogeneous yielding and/or phase transition [37–39]. Further experimental evidence for microscopic heterogeneous deformation is presented by an *in situ* flash X-ray observation of shock-deformed single crystals [40]. Shock-recovery experiments of single crystal anorthite subjected to shock compression show the intergrowth textures of diaplectic glass and anorthite crystal [41]. It is recognized that these textures are caused by macroscopic heterogeneous deformation and the subsequent heterogeneous temperature distribution. The heterogeneous deformation for brittle materials also strongly affects reconstructive phase transition and dissociative reaction, for example, in forsterite to an assemblage of MgO plus $MgSiO_3$ perovskite [42].

In order to estimate such a heterogeneous temperature distribution, we propose the following simple model, namely the skin model. It is assumed for simplicity that the initial powder aggregates are transformed to closely packed cubes with a relatively thin skin through a shock front, as shown in Fig. 11. Consequently, we consider that the three stages in shock compaction process are already achieved in the shock front, in which the powder particles are re-stacked, yielded and/or fractured, and compressed [2, 3, 43]. Jetting from the particle surface into the pore must also be happening in the shock front. Such phenomena depend on shock pressure, initial particle size, initial density, and so on, and result in a shock-front structure with a certain thickness and a consequent time duration, for example, more than 100 nsec [44]. When a coarse powder of Al_2O_3 with an average particle size of 300 μm is shock-compacted to nearly theoretical density, the grain size of the powder is reduced to a few micrometres, while particle size reduction for the fine powder of Al_2O_3 with an average size of 3 μm is not so remarkable [45]. In any case, we suppose that the complicated shock process mentioned above can be finished in the shock front and then

the shock-compressed state as shown in Fig. 11 can be achieved after the passage of the shock front. Moreover, since we suppose that the core of the cube is a fragment of the original particle rather than composed of secondarily-joined particles, it is likely that the crystal of the core inside the skin is isentropically compressed or shock-compressed to the full density material without any influences due to the initial porous state. On the other hand, we suppose that the skin includes all the ambiguous effects due to both the initial porous state and the complicated shock process mentioned above. Since the mechanical process propagates with a speed of the order of the shock-wave velocity, all the materials behind the shock front are in mechanical equilibrium and thus shock pressures must be same in both the skin and the core. The thermal process is relatively slower than the mechanical process, and thus it is reasonable that the skin and the core are independent under adiabatic conditions. It is, therefore, possible to divide the total Hugoniot energy of E^* for porous material into components for the skin and the core, where the latter is assumed to be shock-compressed as the crystal material density.

The specific volume (V) at a particular shock pressure can be represented by the following equation with the mass ratio of the skin to the whole (α),

$$V = \alpha V_\delta + (1-\alpha)V_H, \qquad (16)$$

where V_δ and V_H are the specific volumes of the skin and the core, respectively. The mass ratio α is represented as follows:

$$\alpha = 1-(1-2\delta/d)^3 V/V_H, \qquad (17)$$

where δ and d are thickness of the skin and size of the cube as shown in Fig. 11, respectively. The Hugoniot energy E^* for the powder aggregate may be divided into two parts in proportion to the mass ratio because of the adiabatic assumption mentioned above as follows:

$$E^* = \alpha E_\delta + (1-\alpha)E_H, \qquad (18)$$

where E_δ and E_H are the specific energies of the skin and the core, respectively. Since the shock-compressed state for the core can be calculated by using the established Hugoniot for the full density SiC, we can determine the shock state of the skin, namely pressure–volume–temperature relationships, as a function of the ratio of the skin thickness to the cube size (δ/d), using the equations

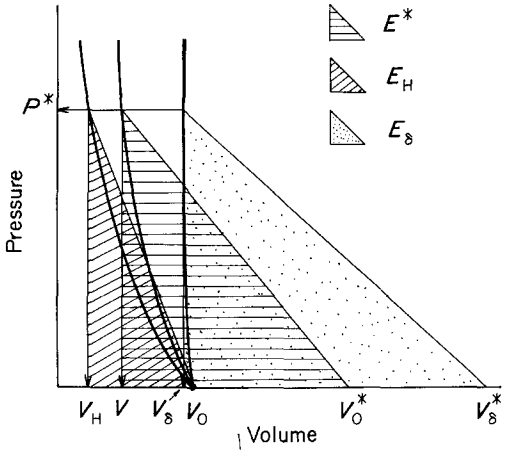

Figure 12 The situation in the pressure–volume plane for the skin model. The subscripts δ and H denote the skin and the core, respectively, while the asterisk denotes the observed or average state.

described in Section 3. The situation in the pressure–volume plane for the skin model is illustrated in Fig. 12.

Calculations for the ratios of the skin temperature to the equilibrium shock temperature and of the skin temperature to the core temperature are performed for some velocity conditions by using the skin model, and shown in Fig. 13 for initial density of 70% and Fig. 14 for 50% initial density. As compared at the same values of δ/d and velocity, the magnitude of the ratio for the 50% initial density is naturally larger than that for 70%. This means that a larger amount of the material in the sample with initial density of 50% will melt compared with the sample of 70% initial density at the same impact velocity. It is, therefore, reasonable that the micro-Vicker's hardness values for the samples initially packed at 50% density are higher than those for samples of 70% initial density at the relatively lower velocity region, although the relative densities of the compacts obtained there by shock compression are not so different. If, however, the reasonable limit in calculation is that V_δ is equal to the specific volume of crystal, the ratio of those temperatures for an initial density of 50% is smaller than for 70%. In any case, the simulation suggests a possibility that the temperature of the skin is approximately one order of magnitude higher than that of the core. The core temperatures in the experimental conditions for the initially packed densities of 50 and 70% are also shown in Table II and in Fig. 10 by the dot-dashed line.

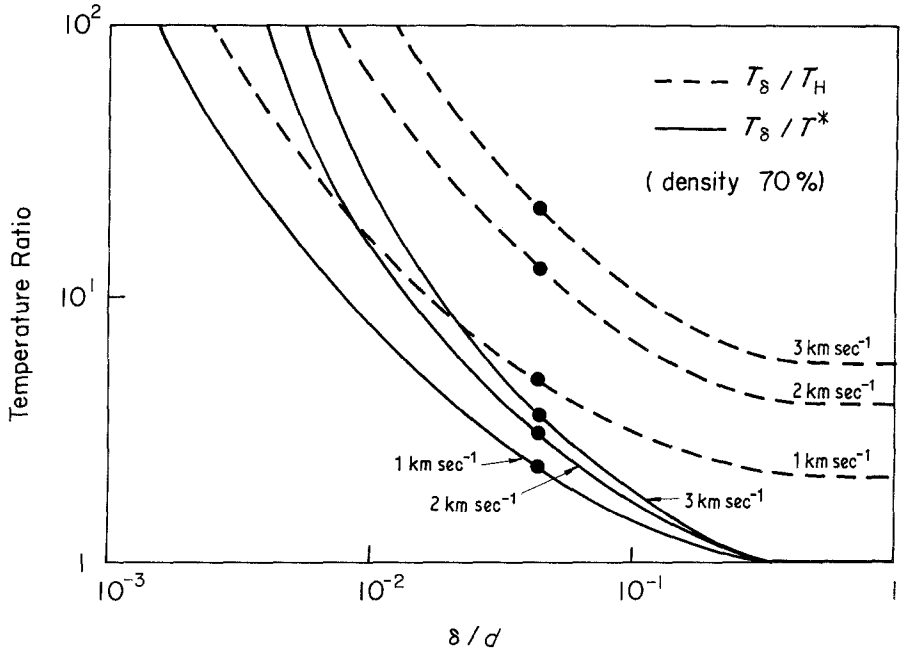

Figure 13 Temperature ratios of the skin to the equilibrium (solid line) and the core (dashed line) as a function of the ratio (δ/d) of the thickness of the skin to the dimension of the cube for an initial density of 70%. The marks on the line indicate that the density of the skin is equal to the crystal density under ambient conditions.

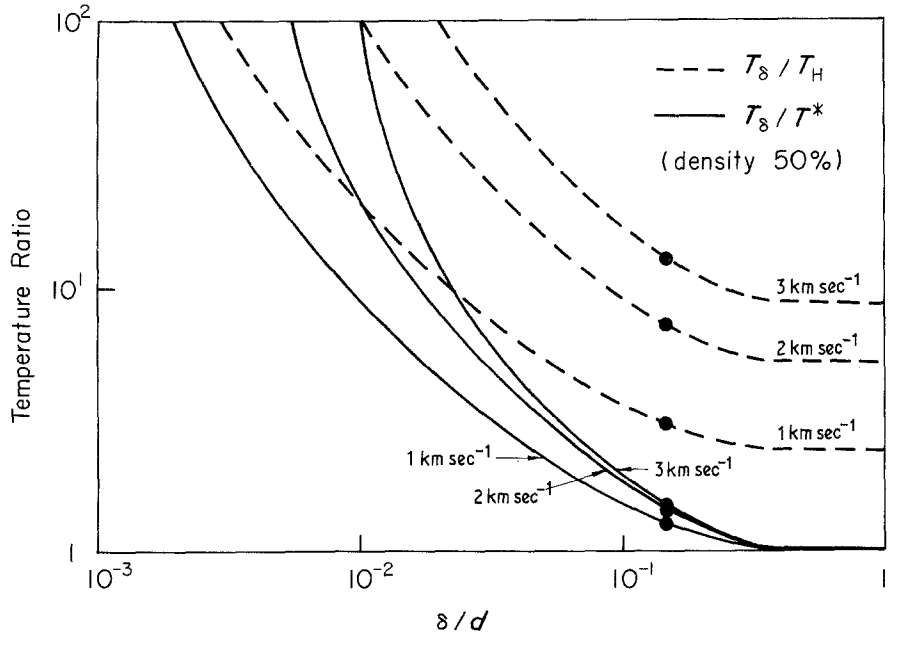

Figure 14 Temperature ratios of the skin to the equilibrium (solid line) and the core (dashed line) as a function of the ratio (δ/d) of the thickness of the skin to the dimension of the cube for an initial density of 50%. The marks on the line indicate that the density of the skin is equal to the crystal density under ambient conditions.

For example, in the actual experimental conditions used to obtain the best compact, the skin temperature is 5340 K at $V_\delta/V_0 = 1$ and then easily exceeds the melting temperature under high pressure, while the core temperature and the equilibrium temperature are 355 and 1780 K, respectively. The ratios of the skin temperature to the core and the equilibrium temperatures are of approximately 16 and 3 times, respectively. For the sample with the unique microstructure as shown in Fig. 8b, the skin temperature and the equilibrium temperature are 3120 and 2200 K, respectively. The former may be higher than the melting temperature and the latter quite close to it. Thus, it is obvious from the skin model that the skin temperature easily exceeds the melting temperature at a value of δ/d around 0.1.

The skin temperature generated should consequently be decreased by thermal diffusion into the core. In the region of $\delta/d \ll 1$, the spatial and time behaviour of an initial "square" temperature distribution at the grain boundary, as shown in Fig. 11:

$$\begin{aligned} T &= T_\delta, \qquad |x| \leqslant \delta, \\ T &= T_{\mathrm{H}}, \qquad |x| > \delta, \end{aligned} \tag{19}$$

is approximately governed by the one-dimensional thermal diffusion equation and solved for an isotropic material as follows [36, 46]:

$$T(x,t) = T_{\mathrm{H}} + \frac{1}{2}(T_\delta - T_{\mathrm{H}}) \left\{ \mathrm{erf}\left[\frac{x/\delta + 1}{2(t/\tau)^{1/2}}\right] - \mathrm{erf}\left[\frac{x/\delta - 1}{2(t/\tau)^{1/2}}\right] \right\} \tag{20}$$

where τ is the relaxation time, given by

$$\tau = \delta^2/D \tag{21}$$

where D is the thermal diffusion constant. The relaxation time is dependent on the thickness of skin and can be estimated approximately by using the thermal diffusion constant in ambient conditions. The relaxation times for several typical materials are shown in Fig. 15 as a function of δ. For SiC, the thermal diffusion constant at 1200° C and atmospheric pressure is used. The line for nonmetallic materials in the figure should be shifted to the left at high temperatures. Since the core is a finite heat sink, the relaxation time shown in Fig. 15 should be of the lower limit value to estimate the thermal relaxation phenomena. The relaxation

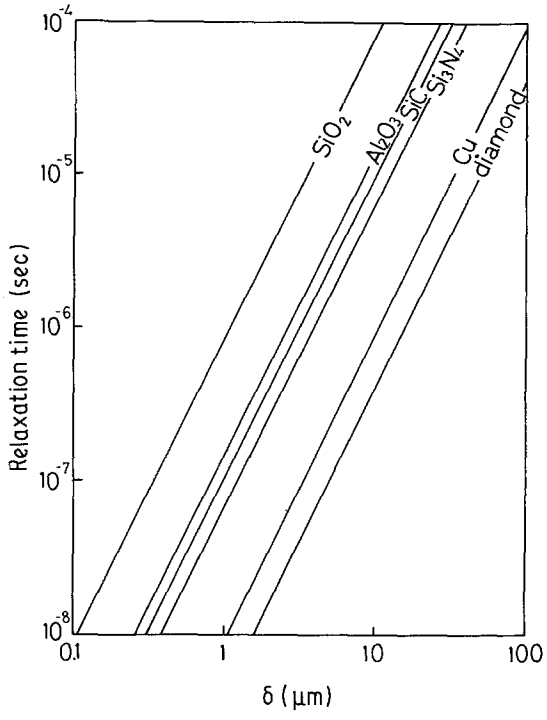

Figure 15 Relaxation times of the skin model for several typical materials as a function of the thickness of the skin (δ). If one substitutes the thickness of the skin (δ) with particle radius, the figure can be used to determine approximately whether or not thermodynamic equilibrium can be achieved during shock loading.

time for SiC at $\delta = 0.1\,\mu$m, which corresponds to the radius of the initial particle, is of the order of 10^{-9} sec and then the large temperature difference between the skin and the core can be almost relaxed in the shock front ($\sim 0.1\,\mu$sec) and also during shock compression ($\sim 1\,\mu$sec). It is reported that the grain size of α-Al_2O_3 with an initially coarse grain size of 300 μm is reduced to a few micrometres by shock loading [45]. In that case, since the relaxation time is comparable with the duration of the shock compression, relaxation phenomena for the temperature difference are critical. Another experiment for SiC using initially coarse grain size is in progress to compare with the results obtained here. In order to apply the skin model to shock compaction and shock consolidation processes, it is necessary to determine the value of the ratio, δ/d. Transmission electron microscope (TEM) analysis can provide the value of the skin thickness which will probably be realized in the coarse grain experiment.

Although this model is a first-order approximation, the idea is fundamental for treating

heterogeneous systems in the case of shock compaction of powders, where mechanical equilibrium can be quickly achieved but thermal equilibrium takes a relatively long time to achieve. This model should be improved to represent the more realistic case in which:

(i) pores still remain at high pressure;
(ii) the skin melts;
(iii) phase transition occurs;
(iv) shock attenuation occurs; and
(v) the compression path in the shock front changes.

For case (i), if we know or assume the real shock compression effect remains in the pores, the Hugoniot energy can be attributed to material only and then the model may be applicable. For cases (ii) and (iii), if we know or can assume the enthalpy and the volume changes for the phase changes and/or also loci of the phase boundary in the pressure–temperature plane, the model is applicable to such multi-phase systems. For cases (iv) and (v), since the mechanical equilibrium process competes with the thermal one, we have to know the precise constitutive relations for a porous system in order to determine the most essential values, namely shock pressure, shock energy, and so on.

5. Conclusions

A well-sintered body of SiC with 97% density and micro-Vicker's hardness of $2700\,kg\,mm^{-2}$ was obtained by the shock compaction technique using a flat-plate impactor. A series of shock compaction experiments using very fine powder with an average size of $0.28\,\mu m$ and systematically changing initial densities and impact velocities, which results in a wide range of shock pressures and temperatures, suggests that the optimum impact condition depends on the initial density. The optimum impact condition in these experiments corresponds to the optimum shock temperature of 1800 K rather than to the shock pressure. The optimum impact condition is $2.5\,km\,sec^{-1}$ for 70% initial density and $2.0\,km\,sec^{-1}$ for 50%. These conditions strongly depend on the material, especially its physical properties, for example, Grüneisen parameter, compressibility and melting temperature. The results of a series of experiments also suggest that disruptive effects must remain in the shock compacted sample, indicated by micro-strain increase and crystallite size reduction, in order to obtain a good compact with high relative density and high strength.

There still remain some serious problems in applying the shock compaction technique to actual ceramic processing, namely induced macro-cracks and remaining pores. The former is caused by both a geometrical problem due to shock reverberations and excess energy due to the excessive velocity impact which is determined in these experiments. Computer simulations using finite difference equations for the conservation relations will aid in the resolution of the geometrical problem [47]. For the latter problem, another initial condition, for example, particle size [45], distribution of the particle size, and remaining or absorbed gas, is important and should be determined with the experiments. The more basic researches to obtain constitutive relations for ceramic powder are necessary for the solution of the latter problem. A precise control of the release process is very important for resolving both problems because pressure and temperature distributions exist in the material under shock loading. The pressure distribution is mainly caused by the geometrical arrangement and is relaxed quickly, while the temperature distribution needs a relatively long time to be relaxed. The skin model is useful in estimating the relaxation phenomena. This model suggests that the thermal relaxation phenomena become critical for grains of small size (a few micrometres) in the ceramic compact under and after shock loading. The size of starting SiC powder used here is too small to apply the skin model and thus the shock temperature can be regarded as the equilibrium temperature. However, since one of the samples is by chance located near to the melting temperature under shock compression, the sample shows the unique microstructure which agrees well with the skin model. Further experiments for SiC powder with an initially coarse grain size are in progress and will be described later.

References

1. R. A. PRÜEMMER, Proceedings of the 4th International Conference of the Center for High Energy Forming, Estes Park (1973) p. 921.
2. S. CLYENS and W. JOHNSON, *Mater. Sci. Eng.* **30** (1977) 121.
3. J. H. ADAIR, R. R. WILLS and V. D. LINSE, "Emergent Process Methods for High Technology Ceramics" edited by R. F. Davis, H. Palmour III and R. L. Porter, Material Science Research, Vol. 17 (Plenum Press, New York, 1984) p. 639.
4. D. RAYBOULD, *J. Mater. Sci.* **16** (1981) 589.
5. D. G. MORRIS, Proceedings of the 4th International

Conference on Rapidly Quenched Metals, Sendai (1981) p. 145.
6. D. G. MORRIS, *Metal. Sci.* (1980) 215.
7. C. F. CLINE, Proceedings of the 4th International Conference on Rapidly Quenched Metals, Sendai edited by T. Matsumoto and K. Suzuki (Japan Institute of Metals, Sendai, 1981) p.129.
8. R. J. CARLSON, S. W. POREMBKA and C. C. SIMONS, *Ceram. Bull.* **45** (1966) 266.
9. C. HOENING, A. HOLT, M. FINGER and W. KUHL, UCRL-79345 (Lawrence Livermore Laboratory, University of California, Livermore, 1977).
10. C. L. HOENING and C. S. YUST, *Ceram. Bull.* **60** (1981) 1175.
11. M. MITOMO and N. SETAKA, *J. Mater. Sci.* **16** (1981) 851.
12. W. H. GOURDIN, C. J. ECHER, C. F. CLINE and L. E. TANNER, UCRL-85274 (Lawrence Livermore Laboratory, University of California, Livermore, 1981).
13. R. K. LINDE and D. N. SCHMIDT, *J. Appl. Phys.* **37** (1966) 3259.
14. W. HERRMAN, *ibid.* **40** (1969) 2490.
15. P. C. LYSNE, *ibid.* **41** (1970) 351.
16. B. M. BUTCHER, "Shock Waves and the Mechanical Properties of Solids", edited by J. J. Burke and V. Weiss (Syracuse University Press, Syracuse, NY, 1971) p. 227.
17. L. SEAMAN, *ibid.*, p. 245.
18. R. R. BOADE, *ibid.*, p. 263.
19. B. D. KRISTOFOROV, L. D. LIVSHITS, I. V. BELINSKY and A. N. AVERIN, *Izv. Phys. Solid Earth* (1971) 549.
20. W. M. ISBELL, "High Pressure Science and Technology" Vol. 1, edited by K. D. Timmerhans and M. S. Barber (Plenum Press, New York, 1979) p. 68.
21. A. SAWAOKA, K. KONDO, N. HASHIMOTO and S. SAITO, Proceedings of the International Symposium on Factors in Densification and Sintering of Oxide and Non-Oxide Ceramics, edited by S. Somiya and S. Saito (Association for Science Documents Information, Tokyo, 1979) p. 339.
22. A. SAWAOKA, K. KONDO and T. AKASHI, *Report Res. Lab. Eng. Mater., Tokyo Inst. Technol.* 4 (1979) p. 109.
23. A. SAWAOKA, S. SOGA and K. KONDO, *J. Mater. Sci. Lett.* 1 (1982) 347.
24. S. SOGA, K. KONDO and A. SAWAOKA, *ibid.* 2 (1983) 673.
25. W. A. RACHINGER, *J. Sci. Instrum.* **25** (1948) 254.
26. H. P. KLUG and L. E. ALEXANDER, "X-Ray Diffraction Procedures" (John Wiley, New York, 1974) p. 618.
27. R. G. McQUEEN, S. P. MARSH, J. W. TAYLOR, J. N. FRITZ and W. J. CARTER, "High-Velocity Impact Phenomena", edited by R. Kinslow (Academic Press, New York, 1970) p. 244.
28. K. KONDO, A. SAWAOKA and T. J. AHRENS, *J. Appl. Phys.* **52** (1981) 5084.
29. J. S. DUGDALE and D. K. C. MacDONALD, *Phys. Rev.* **89** (1953) 832.
30. J. A. VAN VECHTEN, *ibid.* **B7** (1973) 1479.
31. H. SUGIURA, K. KONDO and A. SAWAOKA, *J. Appl. Phys.* **52** (1981) 3375.
32. K. KONDO, A. SAWAOKA, K. SATO and M. ANDO, Shock Waves in Condensed Matter – 1981, edited by W. J. Nellis, L. Seaman and R. A. Graham, AIP Conference Proceedings 78 (American Institute of Physics, New York, 1982) 325.
33. J. CROSNIER, J. JACQUESSON and A. MIGAULT, Proceedings of the 4th Symposium on Detonation (Office of Naval Research, Washington, DC, 1965) p. 627.
34. D. D. BLOOMQUIST, G. E. DUVALL and J. J. DICK, *J. Appl. Phys.* **50** (1979) 838.
35. K. IMAOKA, K. KONDO and A. SAWAOKA, *Jpn. J. Appl. Phys.* **19** (1980) 1011.
36. K. KONDO and A. SAWAOKA, *J. Appl. Phys.* **52** (1981) 1590.
37. K. KONDO and T. J. AHRENS, *Phys. Chem. Minerals* 9 (1983) 173.
38. D. E. GRADY, *J. Geophys. Res.* **85** (1980) 913.
39. Y. HORIE, *Phys. Rev.* **B21** (1980) 5549.
40. K. KONDO, A. SAWAOKA and S. SAITO, "High Pressure Science and Technology" Vol. 2, edited by K. D. Timmerhaus and M. S. Barber (Plenum Press, New York, 1979) p. 905.
41. Y. SYONO, T. GOTO, Y. NAKAGAWA and M. KITAMURA, "High Pressure Research: Application in Geophysics" (Academic Press, New York, 1977) p. 477.
42. Y. SYONO, T. GOTO, H. TAKEI, M. TOKONAMI and K. NOBUGAI, *Science* **214** (1981) 177.
43. M. J. DONACHIE, Jr. and M. F. BURR, *J. Metals* **15** (1963) 849.
44. T. TANIGUCHI, MSc thesis, Tokyo Institute of Technology (1984).
45. R. A. PRUMMER and G. ZIEGLER, *Powder Metallurgy Int.* 9 (1977) 11.
46. H. S. CARSLAW and J. C. JAEGER, "Conduction of Heat in Solids" 2nd edn (Oxford University Press, Oxford, 1959).
47. M. L. WILKINS and C. F. CLINE, UCRL-86599 (Lawrence Livermore Laboratory, University of California, Livermore, 1981).

Received 2 April
and accepted 10 May 1984